An auroral oval at the footprint of Saturn's kilometric radio sources, colocated with the UV aurorae

Laurent Lamy, Baptiste Cecconi, Renée Prangé, Philippe Zarka, Jonathan D. Nichols, John T. Clarke

▶ **To cite this version:**

Laurent Lamy, Baptiste Cecconi, Renée Prangé, Philippe Zarka, Jonathan D. Nichols, et al.. An auroral oval at the footprint of Saturn's kilometric radio sources, colocated with the UV aurorae. Journal of Geophysical Research Space Physics, 2009, 114, pp.10212. ⟨10.1029/2009JA014401⟩. ⟨hal-03732619⟩

HAL Id: hal-03732619

https://hal.science/hal-03732619v1

Submitted on 25 Aug 2022

HAL is a multi-disciplinary open access archive for the deposit and dissemination of scientific research documents, whether they are published or not. The documents may come from teaching and research institutions in France or abroad, or from public or private research centers.

L'archive ouverte pluridisciplinaire **HAL**, est destinée au dépôt et à la diffusion de documents scientifiques de niveau recherche, publiés ou non, émanant des établissements d'enseignement et de recherche français ou étrangers, des laboratoires publics ou privés.

Copyright - All rights reserved

An auroral oval at the footprint of Saturn's kilometric radio sources, colocated with the UV aurorae

L. Lamy,[1,2] B. Cecconi,[1] R. Prangé,[1] P. Zarka,[1] J. D. Nichols,[3] and J. T. Clarke[4]

Received 28 April 2009; revised 10 July 2009; accepted 20 July 2009; published 24 October 2009.

[1] Similarly to other magnetized planets, Saturn displays auroral emissions generated by accelerated electrons gyrating around high-latitude magnetic field lines. They mainly divide in ultraviolet (UV) and infrared (IR) aurorae, excited by electron collisions with the upper atmosphere, and Saturn's kilometric radiation (SKR), radiated from higher altitudes by electron-wave resonance. Whereas spatially resolved UV and IR images of atmospheric aurorae reveal a continuous auroral oval around each pole, the SKR source locus was only indirectly constrained by the Voyager radio experiment to a limited local time (LT) range on the morningside, leading to interpretation of the SKR modulation as a fixed flashing light. Here, we present resolved SKR maps derived from the Cassini Radio and Plasma Wave Science (RPWS) experiment using goniopolarimetric techniques. We observe radio sources all around the planet, organized along a high-latitude continuous auroral oval. Observations of the Hubble Space Telescope obtained in January 2004 and January 2007 have been compared to simultaneous and averaged Cassini-RPWS measurements, revealing that SKR and UV auroral ovals are very similar, both significantly enhanced on the dawnside. These results imply that the SKR and atmospheric aurorae are triggered by the same populations of energetic electron beams, requiring a unified model of particle acceleration and precipitation on Saturn.

Citation: Lamy, L., B. Cecconi, R. Prangé, P. Zarka, J. D. Nichols, and J. T. Clarke (2009), An auroral oval at the footprint of Saturn's kilometric radio sources, colocated with the UV aurorae, *J. Geophys. Res.*, *114*, A10212, doi:10.1029/2009JA014401.

1. Introduction

[2] As for other magnetized planets, energetic electron beams (accelerated to a few keV) flowing along polar magnetic field lines generate auroral emissions at Saturn. They consist of ultraviolet (UV) [*Judge et al.*, 1980; *Clarke et al.*, 1981] and infrared (IR) [*Stallard et al.*, 2008a] aurorae, excited by electron collisions with the upper atmospheric species, and of Saturn's kilometric radiation (SKR) [*Kaiser et al.*, 1980], radiated from higher altitudes through Cyclotron Maser Instability (CMI) [*Wu*, 1985; *Galopeau et al.*, 1989; *Zarka*, 1998]. Contrary to spatially resolved sources of UV and IR aurorae, radio sources could not be directly localized because of the lack of angular resolution at kilometric wavelengths.

[3] However, measurements of SKR flux and polarization by the Planetary Radio Astronomy (PRA) experiment, on board the Voyager spacecraft [*Kaiser et al.*, 1980], allowed the indirect constraint of the SKR source locus, the emission being strongly anisotropic, by analyzing the visibility conditions of the SKR along the spacecraft path. By contrast with the UV and IR aurorae, both organized along a narrow continuous auroral oval around each pole [*Trauger et al.*, 1998; *Cowley et al.*, 2004; *Gérard et al.*, 2004] at $\sim 70°$–$75°$ latitude, with subcorotating hot spots [*Badman et al.*, 2006; *Grodent et al.*, 2005], generally more intense on the dawnside [*Clarke et al.*, 2005; *Stallard et al.*, 2008b], the radio sources were found to have a maximum probability for local times (LT) within the morning-to-noon sector, at latitudes above 60°, with north-south conjugacy [*Kaiser et al.*, 1984; *Galopeau et al.*, 1995]. The radio aurorae were thus suspected to be fixed in LT, leading to interpret the SKR modulation as a fixed flashing light, triggered by "something" rotating with the planet. In order to explain the SKR LT dependence, specific models of charged particle acceleration along magnetic field lines were developed [*Kaiser et al.*, 1984; *Galopeau et al.*, 1995; *Southwood and Kivelson*, 2009], different from those established for the UV/IR aurorae, a rather nonphysical situation.

[4] The arrival of the Cassini spacecraft at Saturn in July 2004 provided the opportunity to investigate the SKR source location more in depth using the capabilities of the RPWS experiment [*Gurnett et al.*, 2004] in various ways.

[1]LESIA, Observatoire de Paris, UPMC, CNRS, Université Paris Diderot, Meudon, France.
[2]Space and Atmospheric Physics Group, Blackett Laboratory, Imperial College London, London, UK.
[3]Department of Physics and Astronomy, University of Leicester, Leicester, UK.
[4]Center for Space Physics, Boston University, Boston, Massachusetts, USA.

Copyright 2009 by the American Geophysical Union.
0148-0227/09/2009JA014401

First, the large variety of orbits allowed us to observe the SKR from all spacecraft LT [*Lamy et al.*, 2008a], suggesting a source region significantly extended in LT. Second, simulations of SKR visibility compared to RPWS dynamic spectra revealed that SKR arc-shaped structures in the time-frequency plane can result from hot spots in partial corotation, and that equatorial and high-latitude extinction zones require radio sources distributed at all LT and at high latitudes. Both features are reminiscent of UV auroral emissions [*Lamy et al.*, 2008b; *Lamy*, 2008].

[5] Then, the goniopolarimetric capabilities of the RPWS High Frequency Receiver (HFR) made it possible to directly determine the SKR Stokes parameters (flux and full polarization state) of observed radio waves and their direction of arrival [*Cecconi and Zarka*, 2005]. Similar "direction-finding" techniques, developed since the 1980s for space observations of the Earth's auroral kilometric radiation (AKR), resulted in the direct mapping of a few AKR events down to discrete UV auroral sources [*Huff et al.*, 1988; *de Feraudy et al.*, 1988; *Panchenko*, 2003; *Mutel et al.*, 2004]. Twenty years later, RPWS/HFR goniopolarimetric results were used to infer the SKR source location quasi-continuously. The first results, based on a perikrone time interval, indicate SKR sources concentrated along high-latitude magnetic field lines and encompassing all LT, including dusk and night, at odds with earlier understanding [*Cecconi et al.*, 2009].

[6] Finally, recent studies [*Kurth et al.*, 2005; *Lamy*, 2008] independently suggest some temporal correlation of the radio and UV auroral fluxes, as in the case of Jupiter [*Prangé et al.*, 1993], both triggered by the solar wind.

[7] In this article, we present improved goniopolarimetric distributions of SKR sources derived by identifying the "active" magnetic field lines, mapping the sources down to the ionosphere, and taking into account flux information to build up high-definition instantaneous SKR intensity maps. Section 2 investigates direct comparison of auroral radio maps with simultaneous UV images measured by the Hubble Space Telescope (HST) between 13 and 26 January 2007 (DOY 13–26). Then, section 3 displays successive SKR images over an extended period where Cassini had a good visibility on radio sources, revealing the strong link between the location of the observed sources and the position of the spacecraft. Section 4 shows statistical maps built over 3.75 years of SKR observations and around 400 individual UV images acquired over two HST campaigns in January 2004 and January 2007. Physical implications are discussed in section 5. The radio imaging technique used to

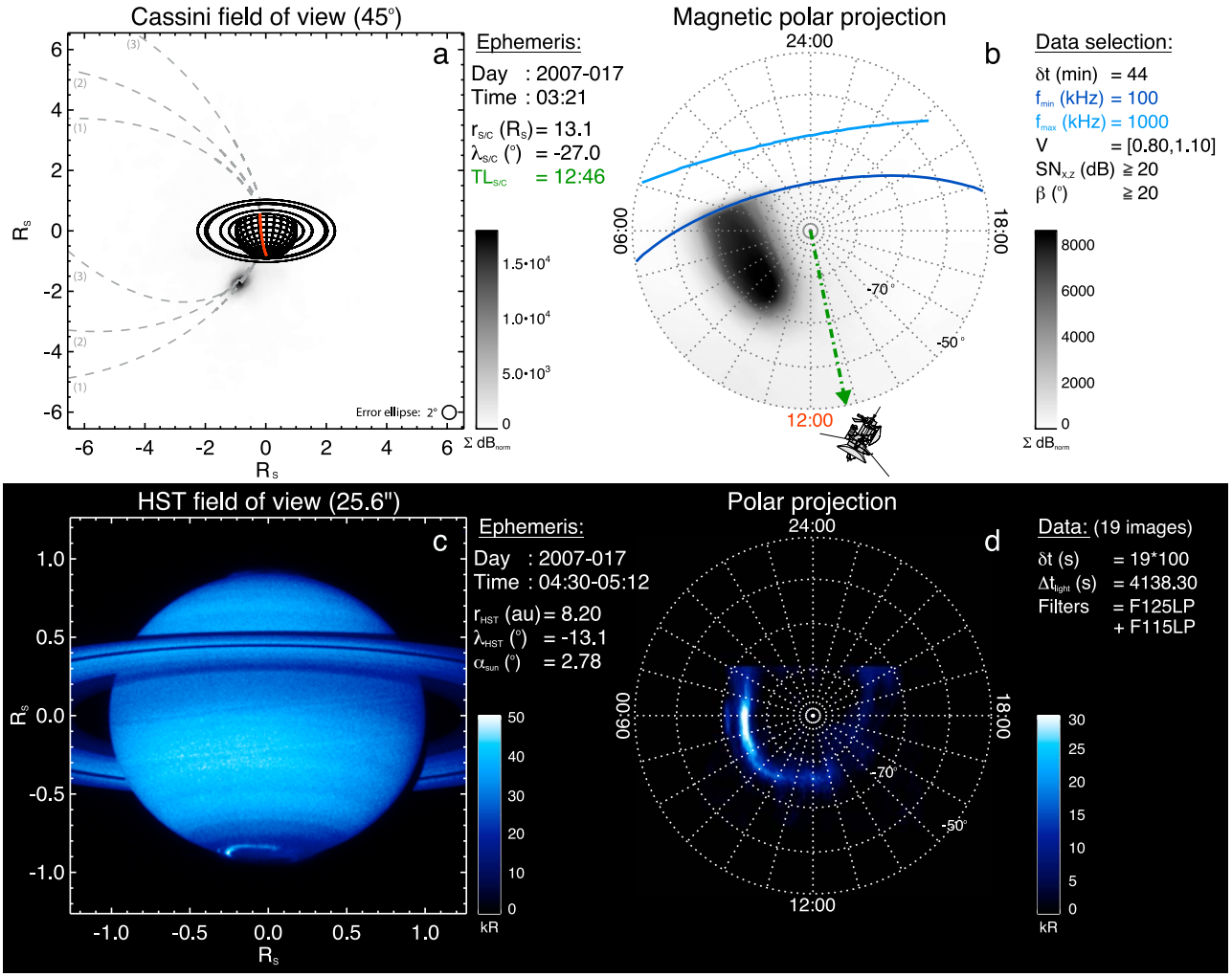

Figure 1

build radio maps displayed in this article is described and discussed in details in Appendix A.

2. SKR Images and Simultaneous UV Aurorae

[8] Whereas the HST campaign of January 2004 corresponded to distant SKR observations (Cassini orbits around Saturn since July 2004), i.e., without resolution on radio imaging, the HST observations of January 2007 provided the opportunity to investigate the location of SKR sources from Cassini-Saturn distances between 12.5 and 28 R_S (one Saturn's radius R_S = 60268 km), and how they do relate to simultaneously observed UV aurorae.

[9] Figures 1a and 1b illustrate the distribution of SKR sources observed on day 17 of January 2007 (hereafter DOY), 0321 to 0405 UT, covering a period when UV images were acquired. During this interval, Cassini and HST had a similar point of view on Saturn's southern pole (LT = 1211 and 1241, respectively). Figure 1a displays the 2-D distribution of SKR sources projected along the direction of arrival onto the observing plane (normal to the Cassini-Saturn direction and including the center of the planet) as derived from the goniopolarimetric analysis. It reveals that most of the sources are clustered below the southern pole region on the left side of the planet. Cassini being close to Saturn's local noon, marked by the red meridian, the sources are thus located on the morning sector along high-latitude magnetic field lines (dashed lines). The 3-D location of radio sources at frequency f is derived [*Cecconi et al.*, 2009] from the intersection of each wave's direction of arrival with the $f = f_{ce}$ surface (f_{ce} being the electron gyrofrequency). Then, a projection along magnetic field lines down to the ionosphere provides the source footprint map (Figure 1b). It reveals, not a localized, but an extended source region in the morning sector, covering the LT range ~0400 (geometric limit of the observable zone) to ~1100, and confined between the $-70°$ and $-80°$ parallels. This specific location does not result from the spacecraft-planet geometric configuration (as demonstrated in Appendix A, section A3) but rather suggests that part of an auroral oval is detected. The corresponding UV image is similarly displayed in the observation plane (Figure 1c) and projected onto a polar view (Figure 1d). Here, all the HST exposures of the day have been summed up (corresponding to 32 effective minutes within the [0430, 0512] UT range), so that the signal-to-noise ratio (SNR) is increased while the morphology is not blurred. The UV images show a thin oval well defined around $-75 \pm 2°$ on the morningside with highest intensities between 0500 and 1000 LT. Its fainter diffuse dusk part reaches latitudes up to $-80°$.

[10] The comparison of Figures 1b and 1d highlights important features: in spite of the low resolution of the radio map (resulting from the large Cassini-Saturn distance; see Appendix A, section A1), a clear relationship appears between the magnetic footprint locus of the radio sources and the most intense UV auroral zone: same latitude range ($-75 \pm 5°$ and $-75 \pm 2°$), and similar LT coverage ([0400, 1100] and [0500, 1000], respectively). The main difference is that UV emissions are detected, although at various intensity levels, at all visible LT (except between 2000 and 0300 LT, beyond the horizon), while Cassini does not detect any duskside or subspacecraft emission.

[11] This does not mean that these locations are devoid of SKR sources. Indeed, each RPWS time-frequency measurement mixes wave signals coming from all directions, and is dominated by the contribution of the most intense sources (here on Saturn's dawn). Also, SKR detection is strongly affected by visibility effects resulting from the anisotropy of the emission [*Lamy et al.*, 2008a, 2008b; *Cecconi et al.*, 2009], radiated along a conical surface centered on the

Figure 1. Auroral emissions observed simultaneously in the radio kilometric (SKR) and UV ranges on 17 January 2007. In order to improve the SNR on the UV data (Figures 1c and 1d) we averaged HST images acquired between 0430 and 0512 UT (see ephemeris of HST to the right of Figure 1d). Radio data (Figures 1a and 1b) correspond to simultaneous two-antenna RPWS measurements (corrected from light travel delay) recorded between 0321 and 0405 UT (see ephemeris of Cassini to the right of Figure 1a) under a severe selection, indicated to the right of Figure 1b, to keep only data of highest quality: f_{min} and f_{max} refer to extremal frequencies, V refers to normalized circular polarization degree, $SN_{X,Z}$ refers to signal-to-noise ratio measured on both dipole X and monopole Z, and β refers to the angle between direction of arrival and antennas plane [*Cecconi and Zarka*, 2005; *Cecconi et al.*, 2009]. Appendix A describes how the radio maps of Figures 1a and 1b are built. Figure 1a displays the SKR sources projected onto the observation plane, using the intensity convention B (see Appendix A, section A2). The resolution of the map is indicated by the 2° disk, and the noon meridian is plotted in red. The sources are well grouped on the southern morningside. Dashed lines (1), (2), and (3) correspond to the projection of high-latitude dawn magnetic field lines (whose footprint coordinates are LT_B = 0500, 0700, and 0900, respectively, and invariant latitude $\lambda_B = -75°$), which cross the source cluster. Figure 1b displays the corresponding SKR polar map (LT, planetocentric latitudes), where intensities are still plotted under the convention B. The blue lines represent the "radio horizons" for the limits of the frequency range, 100 kHz and 1000 kHz. The green arrow indicates the submeridian of Cassini. We observe that the footprints of the SKR sources cover an elongated arc of oval in the range LT = [0400, 1100], between latitudes $-70°$ and $-80°$. Figures 1c and 1d display the UV auroral emission simultaneously recorded with HST, which was close to Cassini's LT ($LT(\alpha_{sun})$ = 1211). Figure 1c displays the image averaged over a series of 19 individual images acquired with the ACS camera, using filters F115LP and F125LP, over a ~45 min period, for a total integration time of ~32 min. UV intensity is expressed in brightness unit of kilo-Rayleighs (kR) of auroral emission radiated by H_2 and H-Ly$_\alpha$. Figure 1d displays the polar view of the average image, assuming an altitude of 1000 km for the auroral sources [*Lamy*, 2008; *Gérard et al.*, 2009], and after subtraction of the reflected background contribution (an empirical background has been computed separately for each filter). The polar projection has been corrected from the phase angle α_{sun} (angle Sun-Saturn-HST) and plotted in LT. Figures 1c and 1d both display a well-defined auroral oval lying at latitudes of $-75 \pm 2°$ on the dawnside, where it is most intense (especially between 0500 and 1000 LT), although fainter emissions are visible at other LT with latitudes increasing toward dusk up to $-80°$, where emission is very faint and diffuse.

magnetic field direction. Emission is recorded only when the observer's direction is along this cone. Radio maps thus generally do not display sources in the subspacecraft meridian, but favor two source regions at both sides of it (see section 3), provided that they are at similar latitudes. This is not the case here, based on the UV oval morphology that displays weak dusk sources but at higher latitudes than dawn ones. Hence, due to instrumental and physical reasons, instantaneous radio images only reveal a fraction of existing sources, which depends on Cassini's location.

[12] We note that the correspondence observed in Figure 1 is preserved over an interval reduced to the duration of one single HST exposure, i.e., 100 s (see Appendix A, section A2). DOY 17 thus provided direct evidence of a strong correlation between UV and SKR source locations when Cassini and HST have nearly the same observing geometry (near noon). Among the SKR data set corresponding to the January 2007 HST campaign, DOY 14 illustrates a completely different situation: HST is still near the noon meridian while Cassini is in the postmidnight sector, nearly in opposition with HST. This orbital configuration still shows a strong correlation between the SKR and the UV source location (see Figure 2), with intense emission observed in the dawnside for both spectral ranges. With respect to Figure 1, resolution of radio maps is lower because of the larger Cassini-Saturn distance ($\sim$16.7 R_S). Again, the nondetection of SKR sources around midnight does not imply the physical absence of radio sources in that region. Indeed, similarly to Figure 1, two factors explain this feature. First, Figure 2c reveals that most intense sources lie on the morningside, and second, with respect to the latter, Figure 2d shows dusk sources toward higher latitudes, implying changes in visibility conditions.

3. Continuous Radio Imaging and SKR Visibility

[13] Examples of radio maps displayed in section 2 were chosen within the HST campaign of January 2007, and, because of large Cassini-Saturn distances during this interval, had intrinsic low resolution. Here, we take advantage of RPWS/HFR quasi-continuous observations of SKR to perform radio imaging over an extended time interval and investigate temporal variation of the detected SKR sources.

[14] Animation S1 displays seven consecutive hours of observation where Cassini had a good visibility on SKR sources of both hemispheres (distances between 3.5 and 6.7 R_S and latitudes between $-21°$ and $-28.3°$) with a short time step (10 min) between consecutive images.[1] Figure 3 shows the corresponding radio maps integrated over the entire interval displayed in Animation S1.

[15] A well-defined oval structure (revealing duskside and nightside sources) is mapped between $-70°$ and $-80°$ parallels along the spacecraft trajectory. Indeed, Animation S1 illustrates that apparent sources follow the varying spacecraft LT as a consequence of the SKR visibility, already noticed for Figures 1 and 2, but along a continuous pattern. This effect is averaged out in Figure 3 where SKR sources are observed between 0000 and 1700 LT and $-65°$ and $-80°$ parallels. Substructures observed within the oval have to be related to dynamic SKR visibility, determined by the source-spacecraft configuration (intrinsic variability of radio source coupled to changing position of Cassini).

[16] Figure 3 confirms and improves the average typical distribution of SKR visible sources noticed by *Cecconi et al.* [2009]. In Figure 3a, detected emission is organized along an "bell-shaped" spatial distribution (materialized by the dashed line) with dominant intensity on one or both sides of Cassini's submeridian (see, e.g., map at 0720 UT in Animation S1). However, fainter SKR sources are sometimes detected all along the bell-shaped distribution, especially around Cassini's submeridian (see images at 0550 or 0640 UT). In such cases, Figure 3b reveals an increased visibility on the auroral region with a continuous and extended part of the radio oval (covering half of all LT for image at 0550 UT), centered on the spacecraft LT.

[17] We note that the particular spatial organization of apparent radio sources in the observation plane highlights the existence of arc-like structures in SKR time-frequency dynamic spectra, in terms of source visibility. This is consistent with modeling work of *Lamy et al.* [2008b] that simulated SKR arcs from subcorotating sources. Indeed, when a magnetic field line populated by individual SKR sources (at all frequencies) passes in front of the spacecraft, the detected emission (corresponding only to a small fraction of all radio sources supported by the considered field line) evolves along the dashed line, resulting in an arc-like structure in the time-frequency plane, the lowest (highest) frequencies corresponding to the highest (lowest) altitudes.

[18] Finally, some scattered emission sometimes also appear (e.g., images at 0240 or 0700), leading to projected sources with unusual latitude. Such sudden changes of the directions of arrival should be considered carefully since they most of the time result either from instrumental limits of radio imaging technique and/or from physical SKR characteristics. The results of goniopolarimetric analytical inversion can be affected by intense interferences, directions of arrival close the antennas plane (characterized by a small β angle, as defined in the caption of Figure 1), low SNR or non purely circularly polarized SKR [*Cecconi et al.*, 2008; *Fischer et al.*, 2009]. Intrinsic properties of radio emissions can also affect the final direction of arrival: low accuracy due to large distances, mixing of several sources with similar intensity, refraction along the ray path, etc. Those factors justify a posteriori the severe selection we applied to data (on frequency range, circular polarization V, β angle and SNR) that allow us to build Figures 1 and 2. In spite of this selection, source locations are from time to time still highly scattered or display well-defined but unusual directions. These peculiar intervals are probably due to the simultaneous occurrence of two or more point-like sources. They must be specifically dealt with when building a statistical image (see section 4).

[19] The interval investigated in Animation S1 offers good visibility conditions on three quarters of the radio oval. Other appropriate periods along the spacecraft trajectory similarly display night sources between 1800 and 0000 LT, generally fainter and more diffuse than on the morningside. This feature is discussed in section 4.

[20] We focused in this section on the typical distribution of SKR sources but instantaneous radio imaging applied to continuous SKR observations should bring new insights to

[1] Animation is available in the HTML.

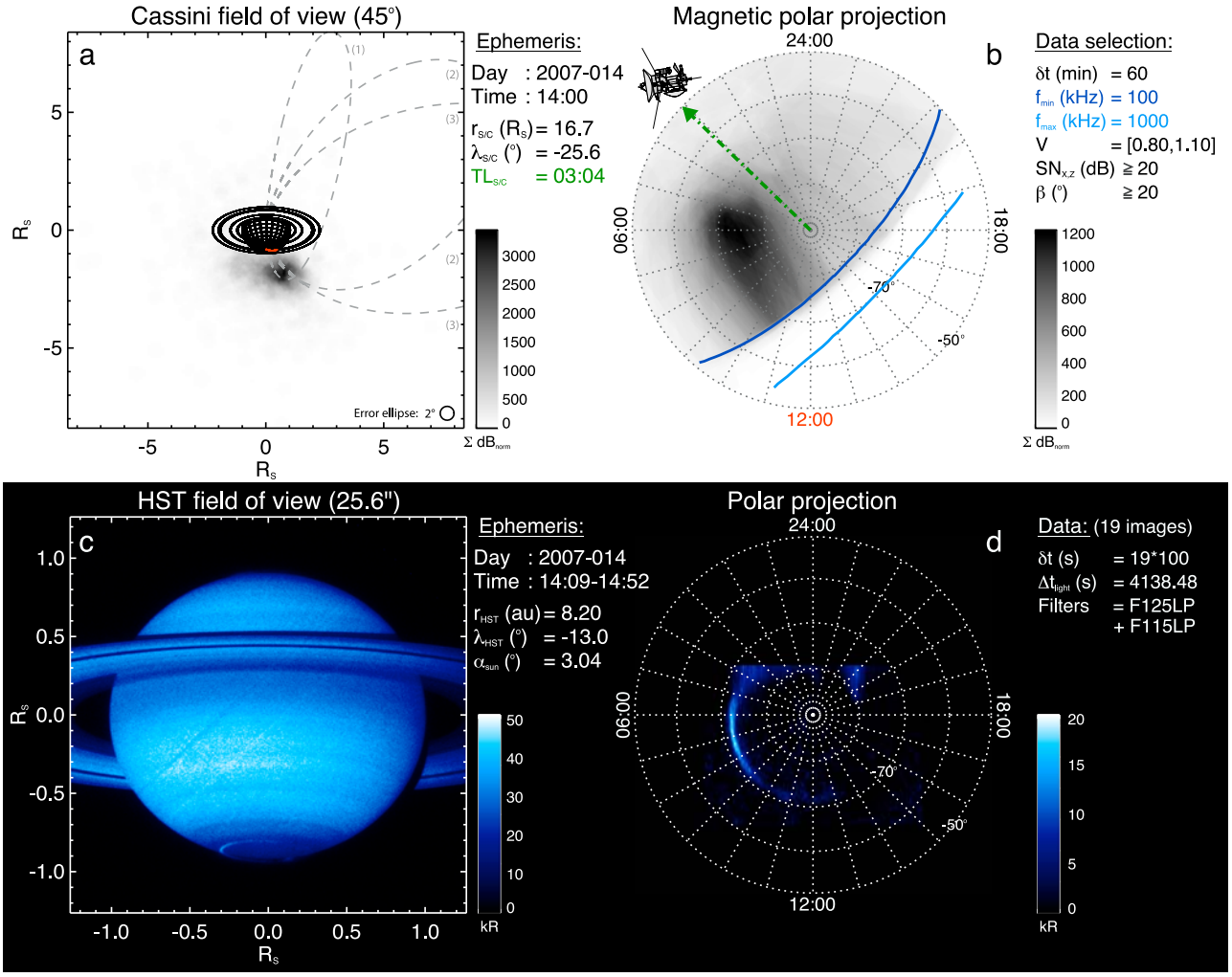

Figure 2. Same as Figure 1 but for day 14 of year 2007 (DOY 14). Here, radio/UV observations are not strictly simultaneous but shifted by approximately 1 h because of weak SKR detected at the HST observing times. HST is near the noon meridian, while Cassini is close to midnight, nearly in opposition with HST. Dashed lines (1), (2), and (3) here display magnetic field lines of invariant latitude $\lambda_B = -75°$ and local times LT_B = 0400, 0600, and 0800, respectively. We observe that the SKR source footprints are more scattered than in Figure 1 (due to larger Cassini-Saturn distance) but concentrate on the morningside, within the LT range [0400, 1100], between latitudes −65° and −85°, consistent with the most intense part of the thin UV oval lying at −72 ± 2°, between 0500 and 1000 LT. UV emissions disappear between 1300 and 1900 LT and are faint elsewhere along the observed oval.

the understanding of the SKR variability. Detailed analysis of motion and modulation of SKR sources is beyond the scope of this paper.

4. Statistical Distribution of Radio/UV Auroral Sources

[21] To push further the investigation of the real distribution of auroral radio sources around the planet, we performed a statistical study based on 3.75 years of SKR observations (between day 181 of year 2004 and day 90 of year 2008) to build the average SKR source locus. The large diversity of Cassini's orbits ensures an exhaustive coverage of all LT, so that any visibility effect should be averaged out.

[22] However, we restricted our analysis to data of highest quality (selection criteria remain identical to those used in previous radio images) and where goniopolarimetric analysis offers good resolution and visibility on radio sources. Constraints have thus been set on Cassini's ephemeris following: $r_{S/C} \leq 15\ R_S$, and latitudes $10° \leq |\lambda_{S/C}| \leq 40°$. The upper limit on the distance is taken to limit the uncertainty on the polar projection resulting from the 2° error ellipse in the observing plane projection. The latitude upper limit corresponds to the value above which SKR polarization becomes elliptical [*Fischer et al.*, 2009] and does not allow us any more to use goniopolarimetric analysis of routine two-antenna measurements (based on the assumption of pure circular polarization [see *Cecconi et al.*, 2009]). The low-frequency limit has been chosen to avoid low-frequency emissions lying below f_{min} = 40 kHz. Then, a set of individual images, with a time step of 10 min, has been built over the whole selected interval. Here, a last

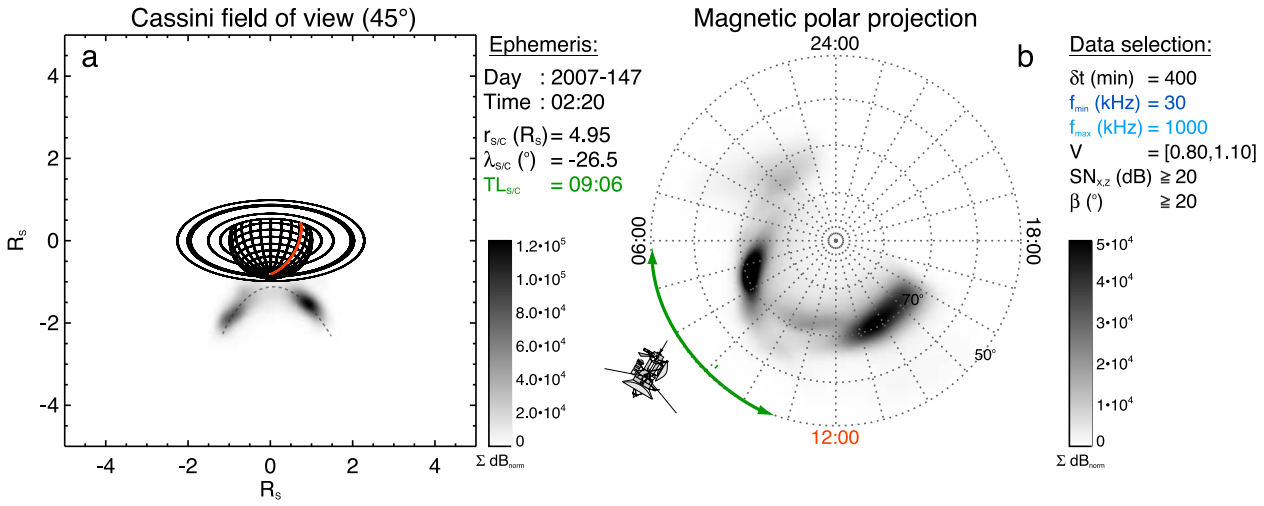

Figure 3. Same as Figures 1a and 1b but integrated over the entire interval displayed in Animation S1. The double-headed green arrow indicates the LT range (0608 to 1034) swept by the spacecraft. The dashed line in Figure 3a marks the typical pattern of the detected SKR sources in the observation plane. Figure 3b reveals an auroral oval observed along the spacecraft trajectory between 0000 and 1700 LT and $-65°$ and $-80°$ parallels.

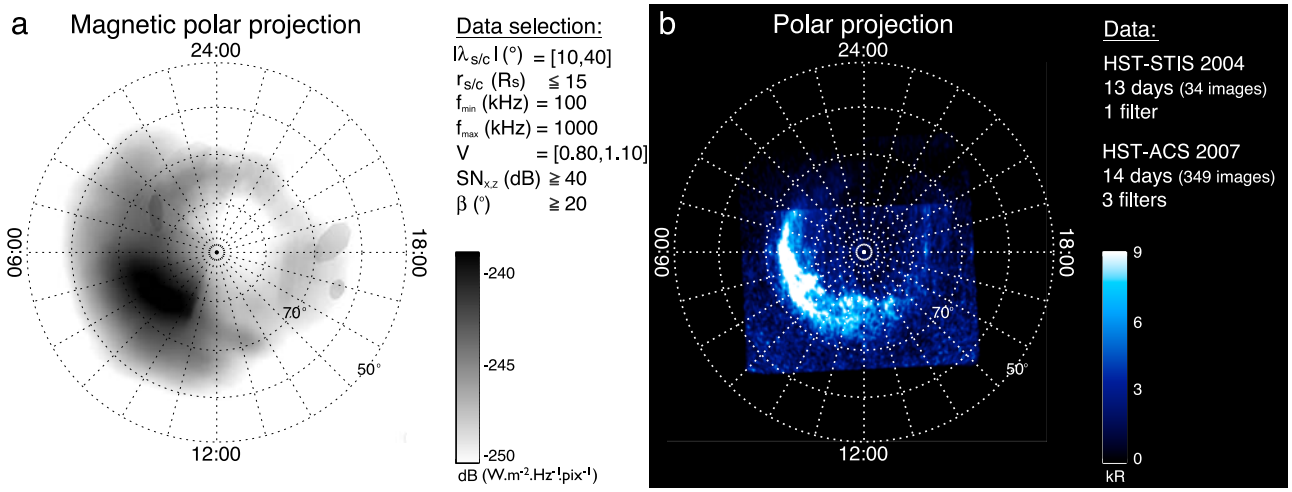

Figure 4. Same as radio/UV polar maps of Figures 1b and 1d, but for a much larger data set. The SKR map (Figure 4a) has been computed with RPWS two-antenna mode (most current one [*Lamy et al.*, 2008a]) recorded between day 181 of year 2004 and day 90 of year 2008 for good visibility conditions: $r_{S/C} \leq 15\ R_S$ and latitudes $10° \leq |\lambda_{S/C}| \leq 40°$, and a strict data selection, indicated to the right of Figure 4b. Then, single images with an integration time of 10 min have been computed under convention A (giving physical intensity; see Appendix A, section A2) over the selected interval. An additional selection has been performed by visual inspection of each single image to remove those most contaminated with highly scattered or unusual emission (see section 3), here corresponding to approximately one third of the inspected data set. The final intensity corresponds to the average computed over all selected single images, covering 23.1 effective days of observations. The structure of the magnetic footprint distribution of the SKR sources is very similar to the UV oval, both in morphology and in intensity. Grey diffuse emission, mainly observed at low morning latitudes, is caused by sporadic dispersed emission (see section 3). The UV statistical oval (Figure 4b) has been computed using a total of 383 individual images from two data sets: 34 STIS images of January 2004 using filter SRF2 (short wavelength cutoff of 125 nm) acquired over 13 days and 349 ACS images of January 2007 using filters LP115, LP125, and LP140 (short wavelength cutoff of 115, 125, and 140 nm, respectively) over 14 days. Reflected background, computed independently for each data set and each filter of STIS-ACS instruments, has been adjusted and substracted on each image and then converted into kR of auroral emission radiated by H_2 and H-Ly$_\alpha$ [*Nichols et al.*, 2008; *Lamy*, 2008]. The final UV oval displays a large latitudinal variability between $-70°$ and $-80°$ and is more intense between ~0500 and ~1200 LT.

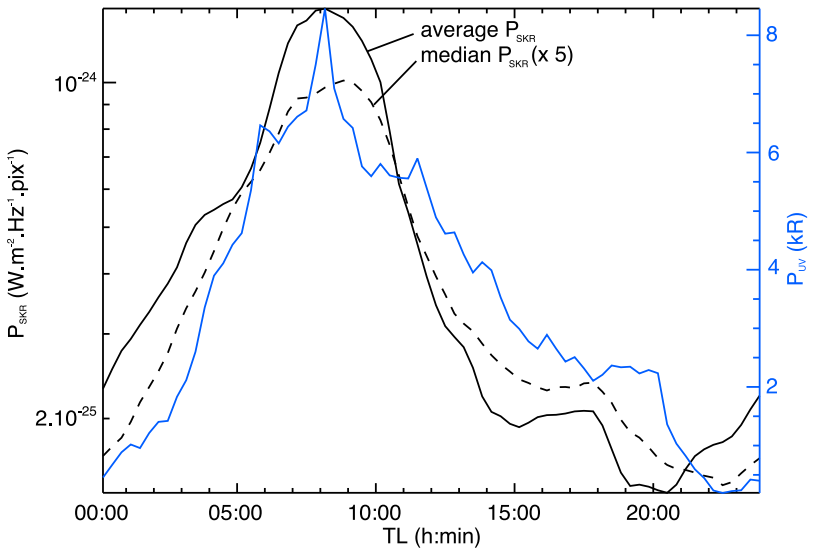

Figure 5. Variations of UV power (blue line) and SKR intensity (black lines) with local time. The solid lines correspond to average intensities of images displayed in Figure 4 between −70° and −80° parallels (where most auroral emissions occur) in bins of 5° longitude. The dashed line is the median SKR intensity (still computed with convention A), less sensitive to the most intense events. The LT variation of the UV power is consistent, even if much less variable, than the one obtained by *Grodent et al.* [2005] with the HST images of January 2004. Measurement errors are smaller that the overall variability of both emissions (with time, hemisphere of origin, visibility, etc.); thus no error bars are shown. UV and radio emissions both peak between 0700 and 0900 LT. Their width at half maximum approximately extends over the ranges [0400, 1400] and [0400, 1200], respectively.

additional selection has been performed by visual inspection of each single image to remove those dominated by highly scattered or unusual emissions (see section 3). The final data set thus corresponds to 23.1 effective days of RPWS measurements.

[23] Figure 4a displays the resulting polar map of SKR source footprints. Results are similar whatever the intensity convention used (see Appendix A, section A2). It reveals a quasi-continuous auroral oval lying at $\lambda_B = -75 \pm 5°$, brightest in the morning sector between 0600 and 1100 LT (similarly to Figure 1) with fainter emissions in the afternoon-to-dusk and premidnight-to-dawn sectors. The broad latitudinal extent of the radio oval reflects both temporal variability of the SKR source location and the cumulated uncertainties of the method (affecting mainly the morningside), discussed in section 3. Implications of this discovery of a radio oval at the footprint of the SKR are discussed below.

[24] We have similarly computed an average UV oval using the HST data from the January 2004 and January 2007 campaigns (representing ∼84% of the entire HST data set obtained before 2007, with around 400 single images), displayed in Figure 4b. The average intensity, expressed in kR, mixes intense UV aurorae of 2004 (observed by STIS) with fainter ones of 2007 (observed by ACS). The UV polar map is strikingly similar to the radio polar map: it displays a continuous auroral oval (less covered for the [2100, 0100] LT sector, where UV sources were beyond the horizon in 2007), covering a large latitudinal extent due to temporal variability, whereas the LT dependence of the output flux remains essentially unchanged.

[25] The latter trend is quantitatively investigated in Figure 5. While the latitudinal variation of both radio and UV ovals is highly variable (southern and northern emissions being mixed in the average radio oval), their variation in LT shows a clear trend that represents a unique feature of Saturn's aurorae. SKR and UV average intensities (black and blue solid lines) have been computed from Figure 4 in bins of 5° of longitude within the [−70°, −80°] latitudinal range, where most auroral sources lie. Additional computation of the SKR median intensity (dashed line) confirms the trend obtained by the average intensity, without being affected by most intense events. The intensity of the SKR sources peaks around 0800 LT and intense SKR sources can be restricted by the width at half maximum to approximately 0400 to 1200 LT, whereas weakest radio sources lie around 2000 LT. The UV power peaks exactly at the same LT than SKR sources, whereas the widths at half maximum defines intense UV sources along the range 0400 to 1400 LT. The difference in the upper limit might result from noisier emission, especially because nightside coverage was missing in 2007. However, a secondary peak appears in both SKR average and median intensities around 1800 LT, roughly matched by a bump in UV power around 1900 LT. This unexpected secondary source region, approximately symmetric to the dawn one with respect to noon, needs to be confirmed with a more extended data set. If persistent, it would indicate a direct generation of accelerated electrons on the duskside.

5. Discussion

[26] The early picture of a flashing auroral radio source roughly fixed in the morning LT sector, derived from spatially unresolved data, is a very crude (and confusing) approximation. The new picture indicates that SKR sources

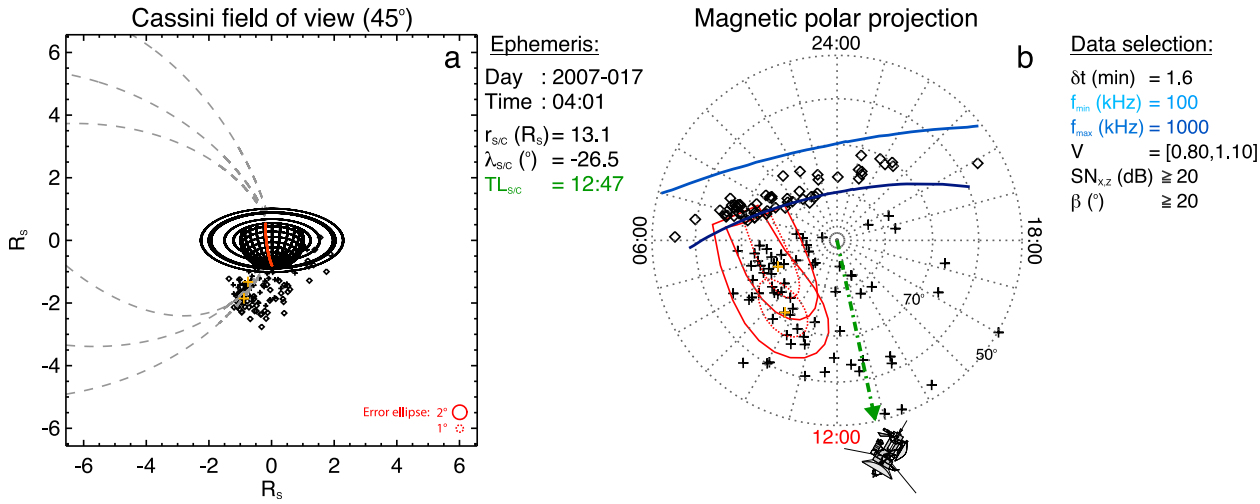

Figure 6. SKR source location observed by Cassini-RPWS over a time interval of 100 s on 17 January 2007 0401, once light time travel (2.6 s) has been corrected. The strict data selection used (identical to that of Figure 1) is indicated to the right of Figure 6b. (a) The distribution of SKR sources in the observation plane. Crosses (diamonds) correspond to directions of arrival at frequency f that intercept (do not intercept) associated isosurface f = f_{ce}. Typical error areas of 1° and 2° are indicated by red circles. Dashed lines are identical to the ones displayed in Figure 1, i.e., display magnetic field lines of invariant latitude $\lambda_B = -75°$ and local times LT_B = 0500, 0700, and 0900, respectively. The red meridian indicates noon. (b) The magnetic polar projection of radio sources in a polar view. The green arrow shows Cassini's submeridian, and radio horizons (in blue) mark theoretical limits of source visibility for extremal frequencies f_{min} = 100 kHz and f_{max} = 1000 kHz. Orange crosses illustrate the correspondence between Figures 6a and 6b for two particular events.

extend along high-latitude magnetic field lines whose footprints follow a near-complete oval around the pole. An extended peak maximum in the predawn-to-noon sector largely dominates over the 0400–1200 LT sector. The morphology of this oval and its intensity distribution are similar to those of the UV aurorae, both in snapshots and in average maps.

[27] This finding strongly suggests that both phenomena are triggered by the same particle beams precipitating from the outer magnetosphere. In particular it implies that Saturn's aurorae are triggered by electrons (the only possible trigger of SKR emissions), confirming a result that was indirectly inferred from UV observations.

[28] Similarly, the properties of electron distributions derived from SKR studies (energy spectrum, angular distribution, etc.) can now be used in the analyses of UV auroral data. Finally, any theoretical model of magnetospheric dynamics and particle acceleration, either relating a solar wind/magnetopause viscous interaction, to the closed/open field line boundary, or to the subcorotating plasma disk, must be checked against both auroral data sets at the same time.

[29] There still remain issues that require further investigation, and which might express differences in the detail of the mechanisms. The overall SKR flux is modulated at the planet rotation period, while the UV flux does not seem to be. Bright spots have been observed to travel along the UV oval at a fraction of the planet rotation period, but the spatial resolution of the radio maps investigated until now has been insufficient to detect isolated bright SKR sources, although there is indirect indication of subcorotating radio sources [*Lamy et al.*, 2008a]. The long-term database of SKR maps now under construction opens broad perspectives for the understanding of SKR dynamics. Hence, it will be a priority to map the broad morning (and possibly dusk) maximum at better spatial resolution in order to check the validity of the interpretation of the SKR modulation by intense dawn sources flashing regularly, and establish whether spatial structures and/or temporal variations exist, which would constrain the triggering mechanism.

[30] Interestingly, UV and radio auroral emissions have been observed and widely studied on the Earth and on Jupiter, but their relationship is poorly investigated. Future studies with the technique used here will tell whether UV and radio planetary aurorae are always associated or whether particular conditions have to be fulfilled (such as, for instance, to be related to solar wind/magnetosphere interactions, or to involve a particular magnetosphere/ionosphere coupling). The magnetospheres of the three planets are quite different so that it would stringently constrain the physical processes at work and allow an important step forward in our understanding.

Appendix A: Building Radio Maps

A1. Location of Radio Sources

[31] Radio observations of the RPWS experiment consist of electric antenna measurements obtained by sweeping the SKR frequency range regularly with time.

[32] Goniopolarimetric analysis allows us to perform radio imaging, both in the projection onto the plane of the

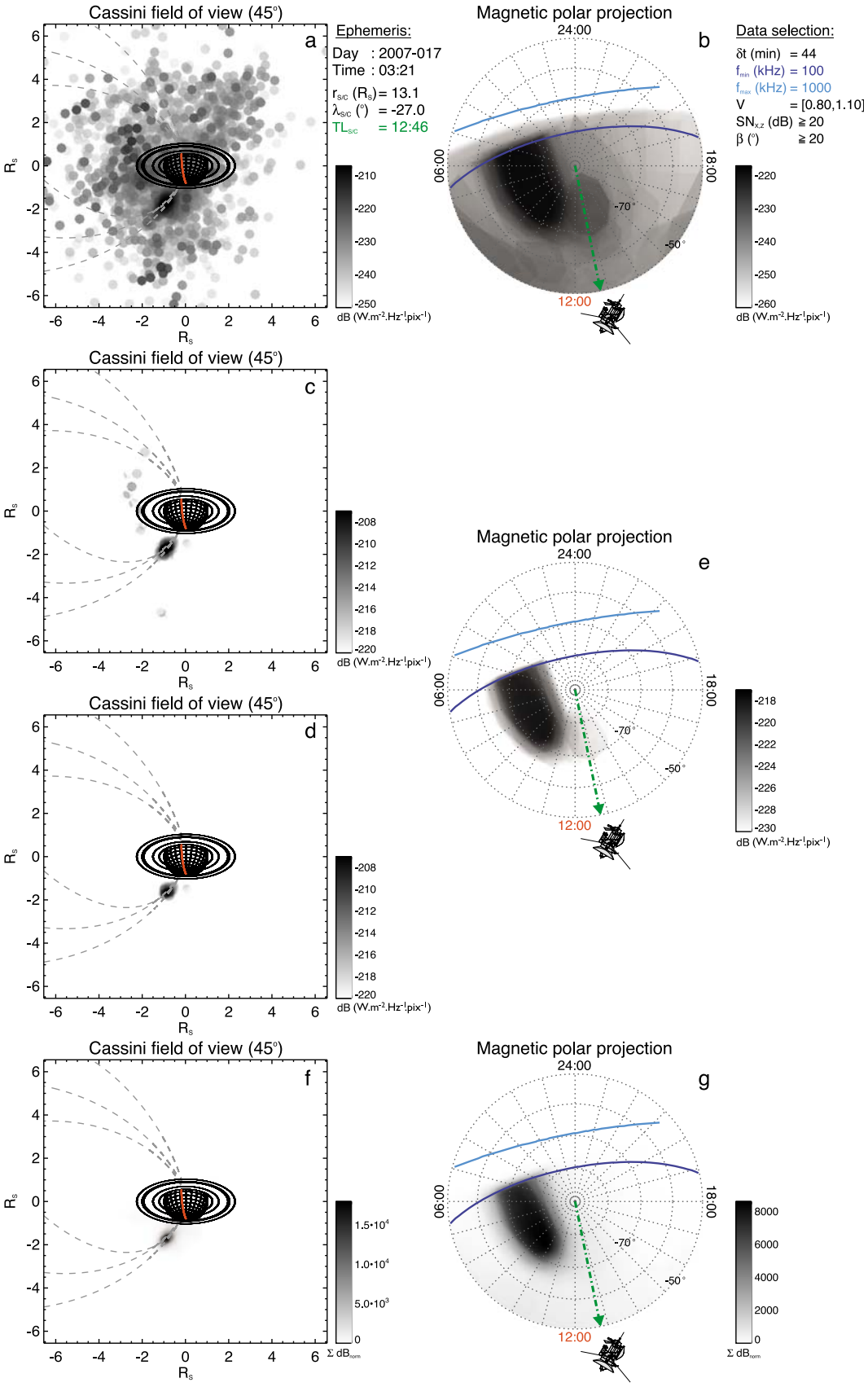
Cassini field of view (45°)
a
Ephemeris:
Day : 2007-017
Time : 03:21
$r_{S/C}$ (R_S) = 13.1
$\lambda_{S/C}$ (°) = -27.0
$TL_{S/C}$ = 12:46
dB (W.m^{-2}.Hz^{-1}.pix^{-1})
Magnetic polar projection
b
Data selection:
δt (min) = 44
f_{min} (kHz) = 100
f_{max} (kHz) = 1000
V = [0.80,1.10]
$SN_{x,z}$ (dB) ≧ 20
β (°) ≧ 20
24:00
06:00
18:00
12:00
-70°
-50°
Cassini field of view (45°)
c
Magnetic polar projection
e
Cassini field of view (45°)
d
Cassini field of view (45°)
f
Magnetic polar projection
g
R_S
Σ dB_{norm}

Figure 7

sky and onto the ionosphere using magnetic polar projections. The latter determination is based on the SPV field model [*Davis and Smith*, 1990] and a simple current sheet [*Connerney et al.*, 1983].

[33] Figure 6 illustrates the construction of such images with plots of the location of directions of arrival (each corresponding to one individual Cassini-RPWS time-frequency measurement) recorded on 17 January and their associated error ellipse.

[34] The method of radio source localization has been described in details by *Cecconi et al.* [2009], and is briefly recalled below. Figure 6a shows the SKR directions of arrival projected along the line of sight in the observation plane of Cassini (normal to the Cassini-Saturn direction and including the center of the planet). Crosses (diamonds) correspond to directions of arrival at frequency f that intercept (do not intercept) associated isosurface $f = f_{ce}$ (f_{ce} being the electron gyrofrequency). It reveals that most of the sources are clustered below the southern pole in the morning sector, along dawnside high-latitude magnetic field lines (dashed).

[35] The 3-D location of radio sources at frequency f is then derived from the intersection of the wave's direction of arrival with the $f = f_{ce}$ surface. Figure 6b shows the polar plot obtained by mapping each SKR source along its magnetic field line down to the planetary ionosphere (so-called magnetic polar projection). The two events, marked by orange crosses, illustrate the correspondence between between Figures 6a and 6b.

[36] The angular uncertainty on each direction of arrival typically varies from 1° to 2° [*Cecconi and Zarka*, 2005]. Hereafter, we keep the largest error estimation of 2°. The associated error area is thus a disk of fixed dimensions in the observation plane (see solid red circle in Figure 6a), whereas its magnetic polar projection is a polygon (see red polygons in Figure 6b) whose dimensions depend on the position of Cassini. Here, projected errors are relatively large because of the large Cassini-Saturn distance ($\sim$13 R_S) combined with the magnetic polar projection effect.

[37] We note that, in both Figures 6a and 6b, events are preferentially observed on the dawnside within latitudes between $-60°$ and $-85°$.

A2. Intensity Conventions

[38] Goniopolarimetric inversions do not only compute the wave's direction of arrival, but also its associated intensity, i.e., the full Poynting vector. Hereafter, we use this double information to build radio intensity maps, with a unique size fixed to 1024×1024 pixels, in which the signal from each individual time-frequency measurement is spread over its associated projected error box (corresponding to the 2° uncertainty discussed in Appendix A, section A1).

[39] Two intensity conventions are discussed below. They are illustrated using the data set of Figure 7 (rather than the one of Figure 6 to include a larger amount of data).

A2.1. Intensity Distribution

[40] Radio maps of Figures 7a–7e display average intensities, obtained from the calibrated intensity of each time-frequency measurement. The intensity related to each pixel i of the final radio map is expressed as

$$S_i = \frac{\sum_j S_{W,j}\delta t_j \delta f_j / N_j}{\sum_j \delta t_j \delta f_j} \quad \text{(A1)}$$

where the RPWS time-frequency measurement j is characterized by its flux S_{Wj} (expressed in W m^{-2} Hz^{-1} normalized to 1 AU [see *Lamy et al.*, 2008a]), its integration time δt_j, its frequency bandwidth δf_j and N_j the number of final pixels covered by its associated error surface (whose shape is a disk in Figures 7a, 7c, 7d, and 7f and a polygon issued from its magnetic polar projection in Figures 7b, 7e, and 7g). The final intensity is consequently expressed in W m^{-2} Hz^{-1} pix^{-1}. This convention is hereafter named convention A.

[41] The final intensity value depends on the resolution of each map (in terms of number of pixels contained in each error ellipse) and thus on the Cassini-Saturn distance. Here, the sources are smeared, especially in latitude, due to the $\sim$13 R_S distance.

[42] Figures 7a and 7b display data plotted over a wide intensity range (whose limiting values are given by the grey scale at the right). It reveals the intrinsic scattering of the emission, even after the severe selection we applied (see caption and summary of data selection at the top right). Nevertheless, emission is clearly enhanced below the southern pole on the morningside (left side).

[43] Figures 7c–7e display restricted intensity ranges to enhance the contrast in favor of the dominant emissions. Whereas Figure 7c plots all selected data (crosses and diamonds in Figure 6), Figure 7d only plots the ones whose direction of arrival intercepts the corresponding iso-f_{ce} (crosses in Figure 6). Only the latter data are used to build up the polar maps of Figure 7e (different from Figure 7b by intensity scale). Figure 7c displays more scattered sources than Figure 7d because it includes the directions of arrival that miss associated iso-f_{ce}, because of the intrinsic uncertainty of goniopolarimetric analysis. To provide maximum information, we will hereafter systematically plot all directions of arrival (crosses and diamonds in Figure 6) for maps

Figure 7. SKR maps using the data of Figure 1 represented with different intensity conventions detailed in Appendix A, section A2. Figures 7a–7e plot average calibrated flux over convention A. Figures 7a and 7b display an intensity scale extending to lower fluxes than those used in Figures 7c–7e. They reveal a large number of events, strongly dispersed, but enhanced along dawnside high-latitude magnetic field lines. The latter feature appears more clearly in Figures 7c–7e, where the intensity range has been stretched to enhance contrast. Following initial data selection, whose criteria are indicated to the right of Figure 7b, all directions or arrival are plotted in Figures 7a and 7c (crosses and diamonds in Figure 6), whereas Figure 7d only plots those that intercept their associated isocontour where $f = f_{ce}$ (crosses in Figure 6). Magnetic polar projections (Figure 7b) and (Figure 7e) are built with the latter data set. Figures 7f and 7g display intensity determined over convention B (occurrence distribution rather than a physical intensity distribution, here more scattered). Organized structures in Figures 7f and 7g are better contrasted than in Figures 7c and 7e.

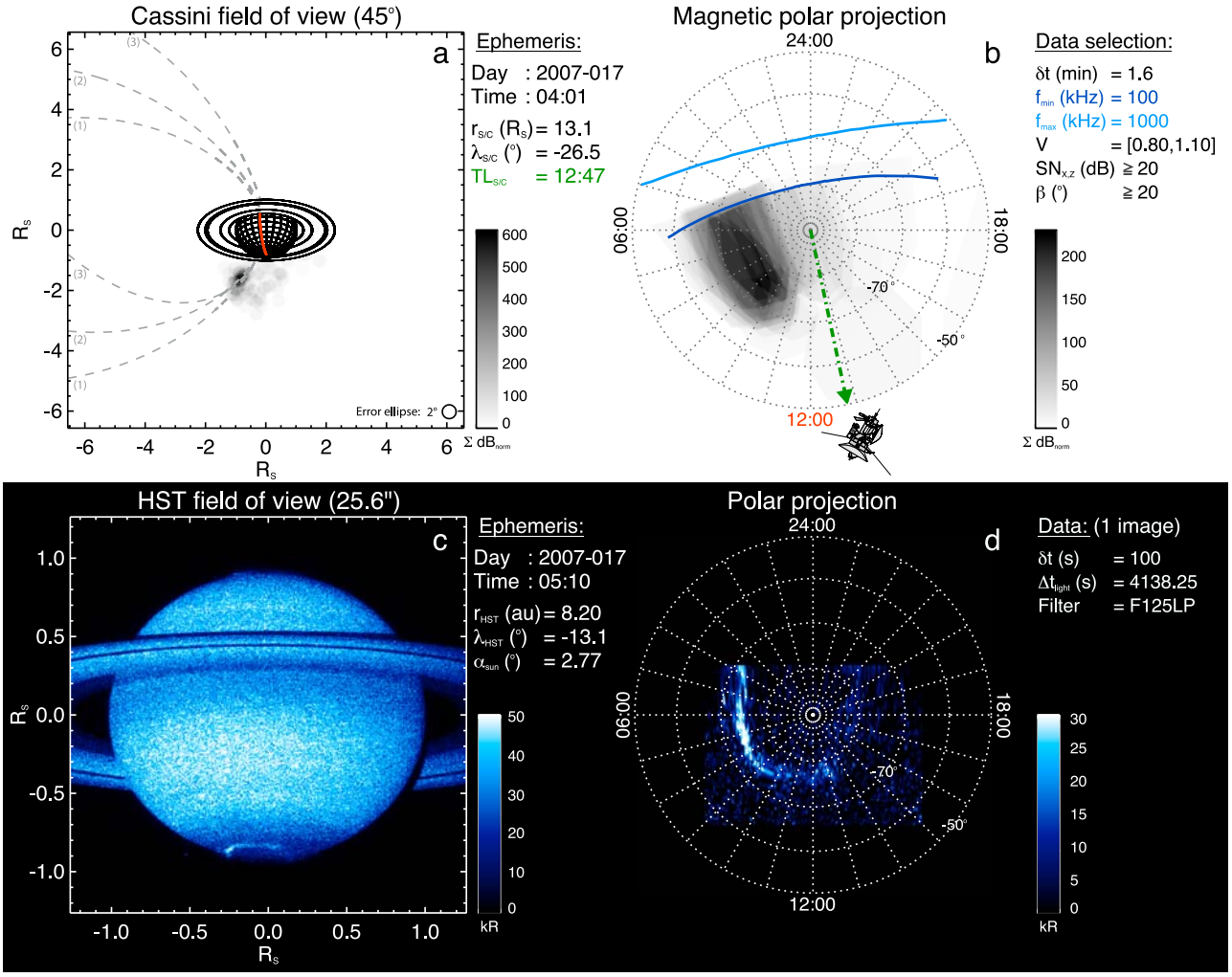

Figure 8. Same as Figure 1 but for a single HST observation of a 100 s exposure acquired on 17 January 2007 at 0510 UT. SKR maps correspond to the SKR data displayed in Figure 6.

in the observing plane, and only those which intersect the iso-f_{ce} surface for polar maps. We must thus keep in mind that the data set between left and right maps is slightly different.

A2.2. Occurrence Distribution

[44] Figures 7f and 7g display a second intensity determination, hereafter named convention B. Here, the intensity affected to each pixel i of the final radio map is expressed as

$$S_i = \sum_j 10 \log \frac{S_{W,j} \delta t_j \delta f_j}{S_0 N_j} \qquad \text{(A2)}$$

where S_0 is a constant reference intensity, arbitrarily taken equal to 10^{-23} J m^{-2}. This particular convention thus represents a product of fluxes over a given threshold, that favors the intersection of error ellipses. It thus emphasizes the locus where most of the sources concentrate rather than the region where the most intense sources lie (occurrence-like distribution rather than energy distribution). Indeed, organized structures in Figures 7f and 7g are better contrasted than in Figures 7c and 7e.

[45] In conclusion, both kind of intensity computations are complementary. Convention A displays average flux in physical units, but is sensitive to intense sources and scattering, possibly due to interferences or related to the spacecraft orientation, whereas convention B lowers the influence of scattered and/or intense sources to identify the region where most emissions originates. In the present paper, we used convention B to built radio maps of sections 2 and 3 (computed over a reduced interval of time, and thus influenced by scattering), and convention A for the statistical radio image displayed in section 4.

[46] Finally, coming back to the example of the data set used in Figure 6, Figure 8 displays radio and UV images of auroral sources, similar to Figure 1, but over a reduced interval, where the time duration of simultaneous UV and radio images is minimum (equal to 100 s). In spite of less intense and more scattered emissions, the correspondence between UV and radio maps is preserved.

A3. Influence of Geometric Bias in Magnetic Polar Projections due to Spacecraft-Planet Configuration

[47] We showed in Figure 6 that magnetically projected errors result in a polygon whose shape and dimensions are

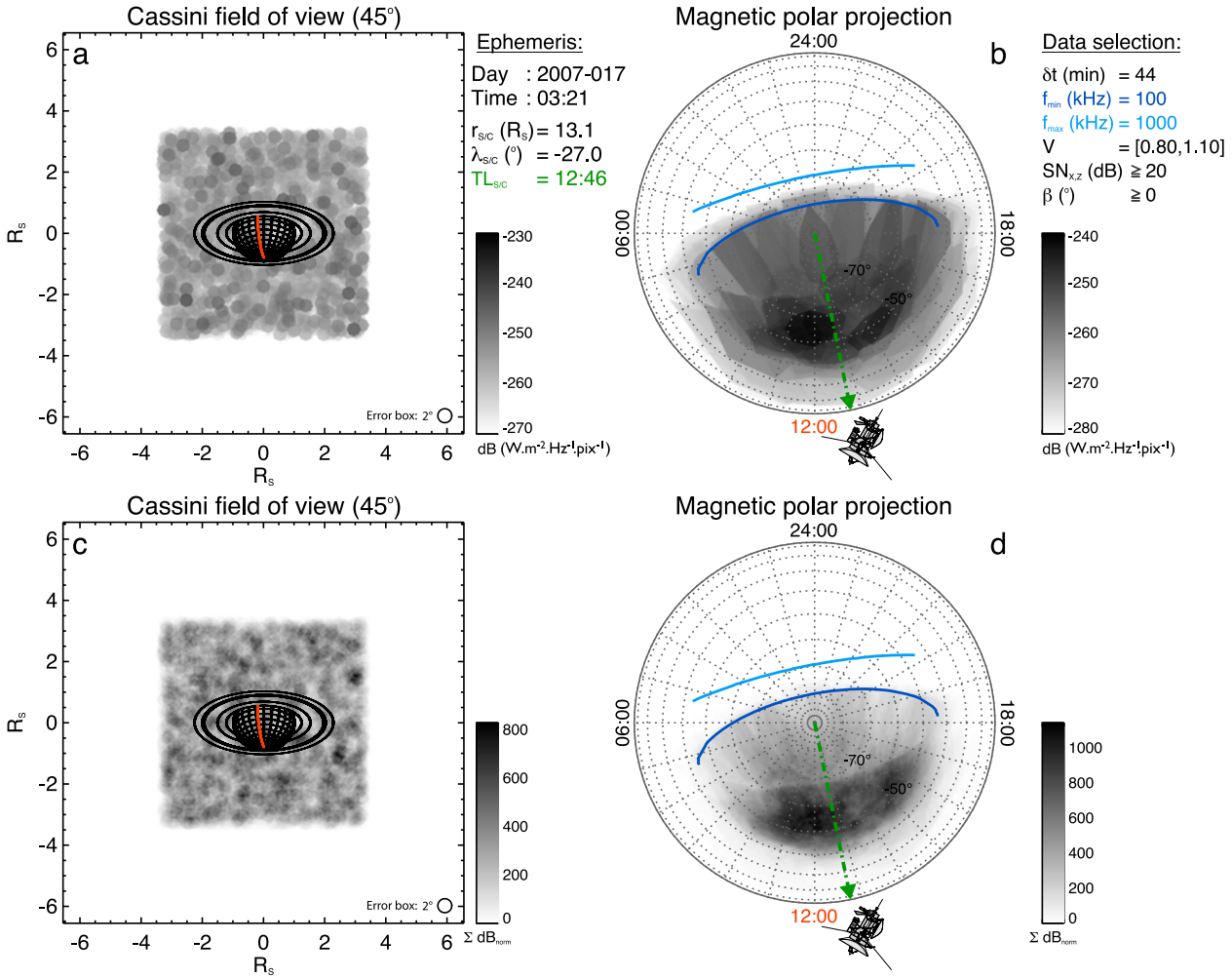

Figure 9. SKR maps derived from the data set of Figures 1 and 7 with the exception that directions of arrival are uniformly random. Figures 9a and 9b use the intensity convention A, whereas Figures 9c and 9d use convention B. Polar maps here plot latitudes down to the equator. Both polar projections display similar results. This Cassini-Saturn configuration should enhance emission around the spacecraft LT and at latitudes between −50° and −70°. However, this geometric bias is not observed in Figures 1 and 7.

linked to the location of the spacecraft. Red error areas in Figure 6b are for instance elongated over the direction of arrival and end at the dark blue radio horizon, plotted for frequency f_{max} = 1000 kHz.

[48] Figure 9 displays numerically simulated radio maps which would result from the data set used in Figures 1 and 7, acquired in the same geometrical conditions, but with uniformly random directions of arrival. It is intended to estimate the influence of the spacecraft-planet geometric configuration on the radio polar maps. The uniform distribution obtained in the observation plane (Figures 9a and 9c) can be used to deduce where emission should geometrically concentrate in the magnetic polar projection. Figures 9a and 9b display the energy distribution A (as in Figures 7a–7e), whereas Figures 9c and 9d display the occurrence distribution B (as in Figure 7). In both cases, the result indicates a peak detection efficiency in the −50° to −60° latitudinal range and on both sides of the meridian of Cassini with a maximum around 1100 LT. At higher latitudes, where SKR emissions are expected, and found (see Figure 1), the simulation shows that the detection efficiency varies smoothly, decreasing from 0500 to 1900 LT, with a small minimum in the late morning-to-noon sector. Consequently, the [0400, 1100] LT section of the radio oval seen in Figure 1 is not subject to a strong geometrical bias (although some extension of the emission region at earlier/later local times cannot be excluded).

[49] **Acknowledgments.** We thank Cassini RPWS engineers at the University of Iowa and the Laboratoire d'Etudes Spatiales et d'Instrumentation en Astrophysique (LESIA) of the Observatory of Paris for support on instrumental questions and ephemeris, and Nicole Letourneur for data processing. L.L. thanks Caitriona Jackman and Cilia Damiani for their help in improving Appendix A, as well as the FPLs for numerous useful discussions. The French coauthors acknowledge support from the Centre National d'Etudes Spatiales (CNES). This work is based on observations with the NASA/ESA Hubble Space Telescope, obtained at the Space Telescope Science Institute, which is operated by AURA for NASA. Work in Boston was supported by grant HST-GO-10862.01-A from the Space Telescope Science Institute to Boston University. J.D.N. was supported by STFC grant PP/E000983/1.

[50] Wolfgang Baumjohann thanks Michael Kaiser and Margaret Kivelson for their assistance in evaluating this paper.

References

Badman, S. V., S. W. H. Cowley, J.-C. Gérard, and D. Grodent (2006), A statistical analysis of the location and width of Saturn's southern aurora, *Ann. Geophys.*, *24*, 3533–3545.

Cecconi, B., and P. Zarka (2005), Direction finding and antenna calibration through analytical inversion of radio measurements performed using a system of two or three electric dipole antennas on a three-axis stabilized spacecraft, *Radio Sci.*, *40*, RS3003, doi:10.1029/2004RS003070.

Cecconi, B., et al. (2008), STEREO/Waves goniopolarimetry, *Space Sci. Rev.*, *136*, 549–563.

Cecconi, B., L. Lamy, P. Zarka, R. Prangé, W. S. Kurth, and P. Louarn (2009), Goniopolarimetric study of the revolution 29 perikrone using the Cassini Radio and Plasma Wave Science instrument high-frequency radio receiver, *J. Geophys. Res.*, *114*, A03215, doi:10.1029/2008JA013830.

Clarke, J. T., H. W. Moos, S. K. Atreya, and A. L. Lane (1981), IUE detection of bursts of H Ly-alpha emission from Saturn, *Nature*, *290*, 226–227.

Clarke, J. T., et al. (2005), Morphological differences between Saturn's ultraviolet aurorae and those of Earth and Jupiter, *Nature*, *433*, 717–719.

Connerney, J. E. P., M. H. Acuna, and N. F. Ness (1983), Currents in Saturn's magnetosphere, *J. Geophys. Res.*, *88*, 8779–8789.

Cowley, S., E. Bunce, and R. Prangé (2004), Saturn's polar ionospheric flows and their relation to the main auroral oval, *Ann. Geophys.*, *22*, 1379–1394.

Davis, L. J., and E. J. Smith (1990), A model of Saturn's magnetic field based on all available data, *J. Geophys. Res.*, *95*, 15,257–15,261.

de Feraudy, H., A. Bahnsen, and M. Jespersen (1988), Observations of nightside and dayside auroral kilometric radiation with viking, in *Planetary Radio Emissions 2*, edited by H. O. Rucker, S. J. Bauer, and B. M. Pedersen, pp. 41–49, Austrian Acad. of Sci. Press, Graz, Austria.

Fischer, G., B. Cecconi, L. Lamy, S.-Y. Ye, U. Taubenschuss, W. Macher, P. Zarka, W. S. Kurth, and D. A. Gurnett (2009), Elliptical polarization of Saturn kilometric radiation observed from high latitudes, *J. Geophys. Res.*, *114*, A08216, doi:10.1029/2009JA014176.

Galopeau, P., P. Zarka, and D. Le Queau (1989), Theoretical model of Saturn's kilometric radiation spectrum, *J. Geophys. Res.*, *94*, 8739–8755.

Galopeau, P. H. M., P. Zarka, and D. Le Quéau (1995), Source location of Saturn's kilometric radiation: The Kelvin-Helmholtz instability hypothesis, *J. Geophys. Res.*, *100*, 26,397–26,410.

Gérard, J.-C., D. Grodent, J. Gustin, A. Saglam, J. T. Clarke, and J. T. Trauger (2004), Characteristics of Saturn's FUV aurora observed with the Space Telescope Imaging Spectrograph, *J. Geophys. Res.*, *109*, A09207, doi:10.1029/2004JA010513.

Gérard, J.-C., B. Bonfond, J. Gustin, D. Grodent, J. T. Clarke, D. Bisikalo, and V. Shematovich (2009), Altitude of Saturn's aurora and its implications for the characteristic energy of precipitated electrons, *Geophys. Res. Lett.*, *36*, L02202, doi:10.1029/2008GL036554.

Grodent, D., J.-C. Gérard, S. W. H. Cowley, E. J. Bunce, and J. T. Clarke (2005), Variable morphology of Saturn's southern ultraviolet aurora, *J. Geophys. Res.*, *110*, A07215, doi:10.1029/2004JA010983.

Gurnett, D. A., et al. (2004), The Cassini Radio and Plasma Wave Investigation, *Space Sci. Rev.*, *114*, 395–463.

Huff, R. L., W. Calvert, J. D. Craven, L. A. Frank, and D. A. Gurnett (1988), Mapping of auroral kilometric radiation sources to the aurora, *J. Geophys. Res.*, *93*, 11,445–11,454.

Judge, D. L., F.-M. Wu, and R. W. Carlson (1980), Ultraviolet photometer observations of the Saturnian system, *Science*, *207*, 431–434.

Kaiser, M. L., M. D. Desch, J. W. Warwick, and J. B. Pearce (1980), Voyager detection of nonthermal radio emission from Saturn, *Science*, *209*, 1238–1240.

Kaiser, M. L., M. D. Desch, W. S. Kurth, A. Lecacheux, F. Genova, B. M. Pedersen, and D. R. Evans (1984), Saturn as a radio source, in *Saturn*, *Space Sci. Ser.*, vol. 9, pp. 378–415, Univ. of Ariz. Press, Tucson.

Kurth, W. S., et al. (2005), An Earth-like correspondence between Saturn's auroral features and radio emission, *Nature*, *433*, 722–725.

Lamy, L. (2008), Study of auroral radio emissions of Saturn, modelling and ultraviolet aurorae, Ph.D. thesis, Observ. de Paris, Univ. Pierre et Marie Curie, Meudon, France.

Lamy, L., P. Zarka, B. Cecconi, R. Prangé, W. S. Kurth, and D. A. Gurnett (2008a), Saturn kilometric radiation: Average and statistical properties, *J. Geophys. Res.*, *113*, A07201, doi:10.1029/2007JA012900.

Lamy, L., P. Zarka, B. Cecconi, S. Hess, and R. Prangé (2008b), Modeling of Saturn kilometric radiation arcs and equatorial shadow zone, *J. Geophys. Res.*, *113*, A10213, doi:10.1029/2008JA013464.

Mutel, R., D. Gurnett, and I. Christopher (2004), Spatial and temporal properties of AKR burst emission derived from Cluster WBD VLBI studies, *Ann. Geophys.*, *22*, 2625–2632.

Nichols, J. D., J. T. Clarke, S. W. H. Cowley, J. Duval, A. J. Farmer, J.-C. Gérard, D. Grodent, and S. Wannawichian (2008), Oscillation of Saturn's southern auroral oval, *J. Geophys. Res.*, *113*, A11205, doi:10.1029/2008JA013444.

Panchenko, M. (2003), Direction finding of AKR sources with three orthogonal antennas, *Radio Sci.*, *38*(6), 1099, doi:10.1029/2003RS002929.

Prangé, R., P. Zarka, G. E. Ballester, T. A. Livengood, L. Denis, T. Carr, F. Reyes, S. J. Bame, and H. W. Moos (1993), Correlated variations of UV and radio emissions during an outstanding Jovian auroral event, *J. Geophys. Res.*, *98*, 18,779–18,791.

Southwood, D. J., and M. G. Kivelson (2009), The source of Saturn's periodic radio emission, *J. Geophys. Res.*, *114*, A09201, doi:10.1029/2008JA013800.

Stallard, T., M. Lystrup, and S. Miller (2008a), Emission-line imaging of Saturn's H3+ aurora, *Astrophys. J.*, *675*, L117–L120.

Stallard, T., et al. (2008b), Complex structure within Saturn's infrared aurora, *Nature*, *456*, 214–217.

Trauger, J. T., et al. (1998), Saturn's hydrogen aurora: Wide field and planetary camera 2 imaging from the Hubble Space Telescope, *J. Geophys. Res.*, *103*, 20,237–20,244.

Wu, C. S. (1985), Kinetic cyclotron and synchrotron maser instabilities—Radio emission processes by direct amplification of radiation, *Space Sci. Rev.*, *41*, 215–298.

Zarka, P. (1998), Auroral radio emissions at the outer planets: Observations and theories, *J. Geophys. Res.*, *103*, 20,159–20,194.

B. Cecconi, L. Lamy, R. Prangé, and P. Zarka, LESIA, Observatoire de Paris, UPMC, CNRS, Université Paris Diderot, 5 Place Jules Janssen, F-92190 Meudon, France. (laurent.lamy@obspm.fr)

J. T. Clarke, Center for Space Physics, Boston University, Boston, MA 02215, USA.

J. D. Nichols, Department of Physics and Astronomy, University of Leicester, Leicester LE1 7RH, UK.